Unsteady Computational Fluid Dynamics Investigation on Inlet Distortion in a Centrifugal Compressor

Armin Zemp
e-mail: zemp@lsm.iet.mavt.ethz.ch

Albert Kammerer

Reza S. Abhari

Laboratory for Energy Conversion (LEC),
Department of Mechanical and Process Engineering,
ETH Zurich,
Zurich 8092, Switzerland

Blade failure in turbomachinery is frequently caused by an excessive resonant response. Forced response of the blades originates from unsteady fluid structure interactions as conditioned in the inlet section by duct bends, struts, or inlet guide vanes. This paper presents the computational part of a research effort that focuses on the blade forced response in a centrifugal compressor. Unsteady fluid flow simulations are used to quantify the forcing function acting on the compressor blades due to inlet flow distortion. The measured inlet flow distribution is applied as inlet boundary conditions in the computation. The unsteady investigation provided the temporal evolution of the distorted flow through the compressor. The time-resolved blade pressure distribution showed the temporal evolution of the dynamic load on the blade surface caused by the inlet distortion. The results suggest that the forcing function is most sensitive in the leading edge region due to inlet angle variations. Toward the impeller stability line the increase in incidence caused separation on the suction side of the main blade and therefore considerably altered the amplitude and the phase angle of the unsteadiness. The investigation of the effect of idealizing the inlet flow distribution on the forcing function showed an increase in the peak amplitude of approximately 30% compared with the actual inlet flow distribution. [DOI: 10.1115/1.3147104]

1 Introduction

Most of the pressure-increasing turbomachines in use are of the radial flow type [1]. Turbomachines using centrifugal effects to increase fluid pressure have been in use for more than a century. The development of centrifugal compressors continued into the 1950s. The demand for advanced military helicopters powered by small gas turbine engines in the 1960s resulted in the further development of the centrifugal compressor. Current feasibility studies by Borgogno and Barmpalias [2] focus on the integration of centrifugals in ultrahigh bypass aeroengines.

In turbomachinery rotating components are subject to vibration. In particular, this applies to rotating blades, which are one of the main contributors to operational failure [3]. Forced response of the blades originates from unsteady fluid structure interaction as conditioned in the inlet section by duct bends, struts, or inlet guide vanes. In industry applications i.e., turbocharging, the inlet section features pipe bends, struts, or guide vanes, which create a nonuniform inlet flow field upstream of the impeller [4]. Such nonuniformities exhibit two main disadvantageous effects: first a deterioration in performance and second the introduction of potential sources of forced response vibration. With regard to the former Cumpsty [5] presented an investigation of a multistage axial compressor and showed that the performance can be seriously affected by inlet distortion. In the latter case resonant vibration of the impeller blades may lead to high-cycle-fatigue failure [6,7].

In the following, the focus will be on vibratory response and the associated problems that require attention during the design phase. In general, the appearance of forced vibration cannot be avoided. For turbocharging applications, in particular, a wide range in rotational speed settings is required, which in turn leads to resonant crossings. From an engineering perspective it is desirable to assess the potential damage to blades caused by forced response vibration, in order to understand the cause of potential failures and to introduce countermeasures. The ongoing development of computational tools offers a wide range of approaches to compute fluid flow and structural mechanics. The recent publication by Dickmann et al. [8] exemplifies potential applications in this regard. By simulating complex flows, excitation acting on the blade surfaces can be assessed and used in life estimation procedures. Moreover, flow analysis allows an improved understanding of the ongoing fluid dynamics that lead to vibration by complementing measurements taken in test facilities or during operation.

2 Scope and Motivation

Forced response is concerned with the pressure and force distributions on the blades and the structural response in terms of deflection and stress distribution. This paper addresses forced response by employing computational fluid dynamics to simulate the flow field upstream and within a centrifugal compressor. The data are intended to quantify the unsteady pressure distribution acting on the blade surface due to inlet flow distortion. The Turbomachinery Laboratory of ETH Zurich operates a centrifugal compressor test rig. Current research activities are aimed toward providing insight into vibratory forced response of a thin bladed impeller. Resonant vibration is generated using distortion screens, which are installed in the inlet section upstream of the impeller. The distortion screens vary in geometry to generate a distinct distortion pattern. In order to quantify the flow properties upstream of the impeller, data acquisition in the inlet flow field is carried out with the so-called fast response aerodynamic probe (FRAP) measurement technique [9,10]. A traversing system allows the movement of the probe in a plane perpendicular to the main flow direction. A detailed specification of the instrumentation and the measurement setup is presented by Kammerer and Abhari [11]. These measured inlet flow quantities were applied as an inlet boundary condition in this unsteady CFD investigation. In

Contributed by the International Gas Turbine Institute of ASME for publication in the JOURNAL OF TURBOMACHINERY. Manuscript received August 25, 2008; final manuscript received September 9, 2008; published online April 2, 2010. Review conducted by David Wisler. Paper presented at the ASME Turbo Expo 2008: Land, Sea and Air (GT2008), Berlin, Germany, June 9–13, 2008.

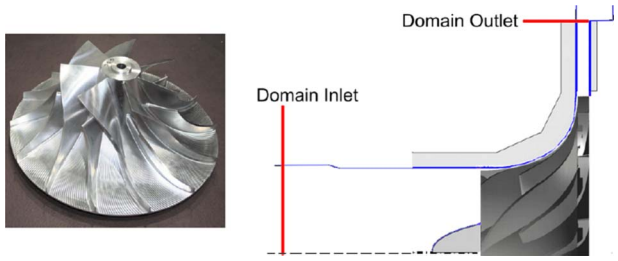

Fig. 1 Impeller and computational domain

the first step, the validation of the numerical model was done on the basis of a cyclically symmetrical model. The data were then compared with the measured test rig performance for the entire operating range. In addition, measured fast response aerodynamic data allowed comparison with the predicted impeller exit flow. In the second step, a time-resolved computation was carried out where the entire impeller was simulated. Idealized and actual inlet boundary conditions were applied. The unsteady computation provided insight into the convection of distorted flow through the impeller and the effect of inlet flow distortion on the blade pressure distribution. An assessment of the blade pressure distribution and its sensitivity to change in mass flow will be presented.

3 Centrifugal Compressor Stage "RIGI"

Experimental data were obtained in the RIGI research compressor facility of the Turbomachinery Laboratory at the Swiss Federal Institute of Technology. The facility consists of a single stage, vaneless industrial centrifugal compressor system operating in a closed loop. The thin bladed impeller used for the investigation is a modified version of the impeller designed by Schleer et al. [12] and has a design pressure ratio of $\pi_0=2.8$ with an outer diameter of 400 mm and a tip clearance ratio $t/b_2=4.5\%$. The impeller features seven full and seven splitter blades whereas the stage consists of a parallel vaneless diffuser with an exit diameter of 580 mm. A large toroidal collecting chamber downstream from the radial diffuser ensures a virtually uniform circumferential pressure distribution at the impeller exit. Figure 1 shows schematically the computational domain used in the present work and a photograph of the impeller.

4 CFD Model and Simulation

4.1 Geometry. The inlet of the computational domain was 2.2 blade heights upstream of the impeller eye. This corresponds to the axial position of the FRAP measurement plane, where inlet flow measurements were performed. The distortion screens were installed about 5.5 blade heights upstream from the impeller inlet. The outlet of the CFD domain coincided with the exit of the diffuser.

4.2 Grid and Flow Solver. The CFD investigation was performed with the commercial ANSYS CFX V10.0 software package [13]. The grid used for the steady state computations consisted of the seventh part of the 7+7 impeller and implemented periodic boundary conditions in circumferential direction. The computational grid for the unsteady investigation represented the entire impeller due to the varying spatial extent of the distinct distortion pattern over the seven main blade pitches and consisted of 4×10^6 nodes that made up 3.5×10^6 hexahedral elements. The grid properties were a trade-off between spatial resolution and the required computational power. One revolution of the impeller was divided into 77 time steps. This yielded a 4.7 deg turn of the impeller for each time step, which was considered to be sufficient to resolve the different inlet distortion patterns and their convection through the compressor stage. For the spatial discretization a second-order scheme was used. Three turbulence models, the $k-\varepsilon$, $k-\omega$, and *SST*, were evaluated. Only the $k-\varepsilon$ turbulence model with scalable wall functions resulted in numerically stable solutions. During steady state computations, both the $k-\omega$ and *SST* turbulence models exhibited poor convergence rates compared with the $k-\varepsilon$ model. Further judgments could be made based on the fact that CFD results showed zones of strong recirculation at the outlet of the computational domain (up to 15% of the outlet area for the *SST* turbulence model). In comparison, these zones of strong recirculation were not present in the FRAP measurements at the outlet of the computational domain. The $k-\varepsilon$ turbulence model was therefore used in the simulations. The maximum residuals in the present work were of the order of 10^{-3} whereas the mass imbalances were found to be in the order of 10^{-6}. The periodicity of the numerical results in the time-resolved computations was quantified via the correlation coefficient of unsteady pressure traces monitored for a number of locations on the main blade surface. The monitoring points were positioned at blade midheight, both on the pressure and suction sides, with the correlation coefficients being computed using data obtained from two consecutive impeller revolutions. It was considered that periodic convergence was reached for a correlation coefficient of 99%, which typically corresponded to six impeller revolutions. Comparable computations were performed by Dickmann et al. [8]; relative to the present work, the computations were prolonged due to the relatively long inlet domain and the associated convection time.

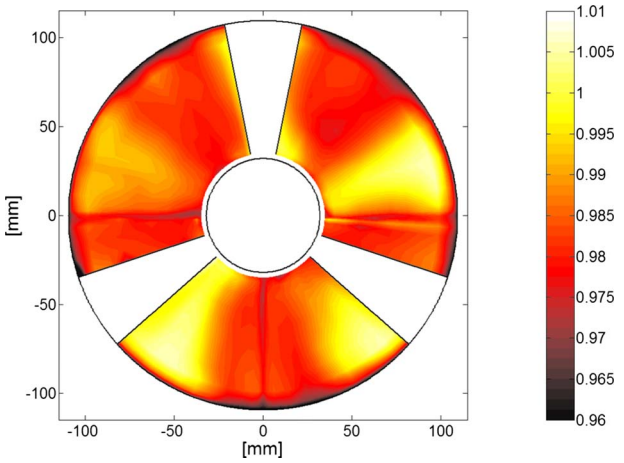

Fig. 2 Measured inlet total pressure distribution p_0/p_{01}

4.3 Boundary Conditions. For the steady state cases, a constant total pressure and total temperature distribution was applied at the inlet of the domain. Data were obtained from performance measurements in the test facility. For the time-resolved cases, measured total pressure and total temperature distributions of the distorted inlet flow field were used as inlet boundary conditions. At the outlet of the domain, for both cases, the average static pressure over the entire outlet area was iteratively adjusted such that the computed mass flow could be matched to the measured mass flows at the corresponding operating point. The measured total pressure distribution is shown in Fig. 2.

The traversing system installed allowed the FRAP probe to be moved in a circumferential as well as in a radial direction. Due to mechanical constrains during traverse measurements, the inlet was partially inaccessible with the probe, as a result of which, data were acquired for 280 deg out of 360 deg of the circumference. The center of the inlet duct was used for strain gauge signal transmission through a slip ring. A detailed description of the measurement setup, as well as a description of the measured flow field, is presented by Kammerer and Abhari [11]. The inlet flow field for the presented case is characterized by a circumferential distortion pattern. Regions of high total pressure correspond to areas where

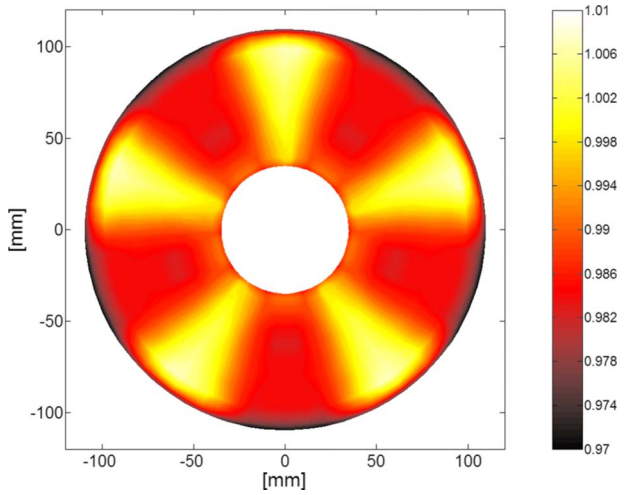

Fig. 3 Interpolated and idealized inlet total pressure boundary condition p_0/p_{01}

axial velocity increases as the fluid passes through the distortion grid. At the outer diameter of the channel regions thick boundary layers can be identified, which stem from deceleration through the distortion grids. In addition the flow field is circumferentially modulated due to support struts within the inlet section. This effect is apparent when comparing the total pressure magnitudes at any radius along a circumferential line. Due to the unavailability of data in the inaccessible portions of the measurement plane, the measured flow distribution was complemented by interpolation in order to obtain a complete distribution over the entire inlet duct area. This flow distribution will be termed "real" and discussed later in the paper.

Further modifications on the inlet flow distribution were performed toward idealization i.e., with the aim that it would resemble an almost sinusoidal excitation in a circumferential direction (Fig. 3).

It was intended to isolate the fundamental frequency of the distortion and its effect on the unsteady pressure distribution on the main blade surface. Therefore, it was possible to deal initially only with the fundamental frequency and to better assess the periodic convergence during the unsteady CFD calculation. In the idealized inlet flow distribution the ratio between the distorted and undistorted flow fields was kept constant in comparison to the real distribution. In the following, computations with an idealized flow distribution will be presented, then a comparison with the real distribution will be made.

4.4 Operating Points for the Unsteady Investigation. The Campbell diagram for the main blade (Fig. 4) shows potential resonant conditions. The natural frequencies of the main blade are shown for Mode 1 to Mode 4 by the curves that show the vibratory response of the main blade at the corresponding rotational speed (shown on the abscissa). The ordinate shows the frequencies of the eigenmodes of the main blade. A potential harmful resonance would occur when the shaft speed dependent engine order intersects the blade eigenfrequency. In the experimental work the excitation of the first main blade mode, indicated as "Mode 1" in the Campbell diagram, was achieved by using a distortion screen with either three, four, or five baffles. The screens with four and five baffles excited the main blade at its fundamental excitation frequency, whereas the screen with three baffles excited with its second harmonic (engine order 6). The operating points of interest for an unsteady CFD investigation were the rotational speeds where the inlet distortion excites the main blade mode and these are marked with circles in the Campbell diagram.

Data presented in this work focus on the results for resonance at

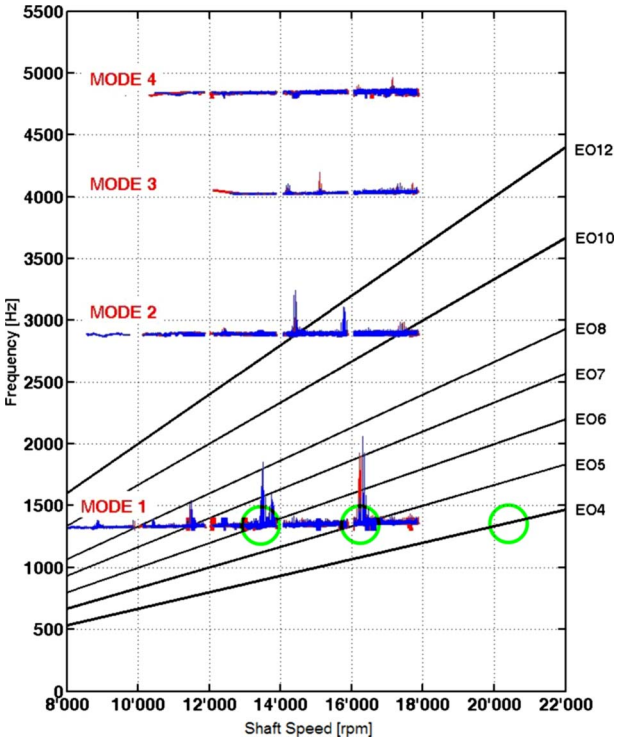

Fig. 4 Campbell diagram of impeller main blade

16,250 rpm and fifth engine order excitation. This excitation order corresponds to the inlet boundary conditions described previously.

5 Steady State Results

Steady state CFD computations of the centrifugal compressor over a broad range of operating points provided a basis to validate the numerical model with performance data measured in the test facility. Both data sets are shown in the compressor map (Fig. 5) and show a reasonable match. The deviation of the calculated performance compared with the measured values was of the order of 2% over the whole operating range. For each speed line, computation was performed such that the static back pressure was increased stepwise toward the stability limit of the compression system. As the stall/surge regime was approached, computation was aborted as soon as steady state convergence could not be achieved. Within the choke regime of the impeller satisfactory results were obtained indicating a good match of the choke mass

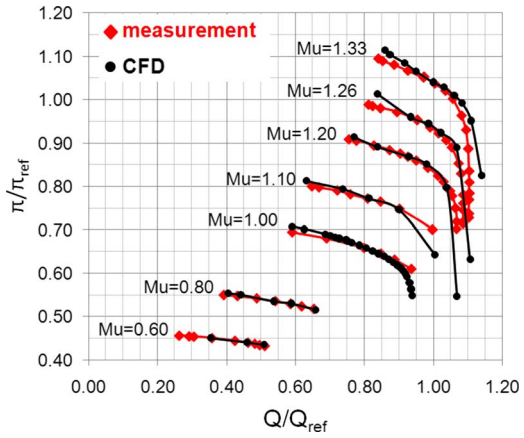

Fig. 5 Compressor map A8C41 impeller

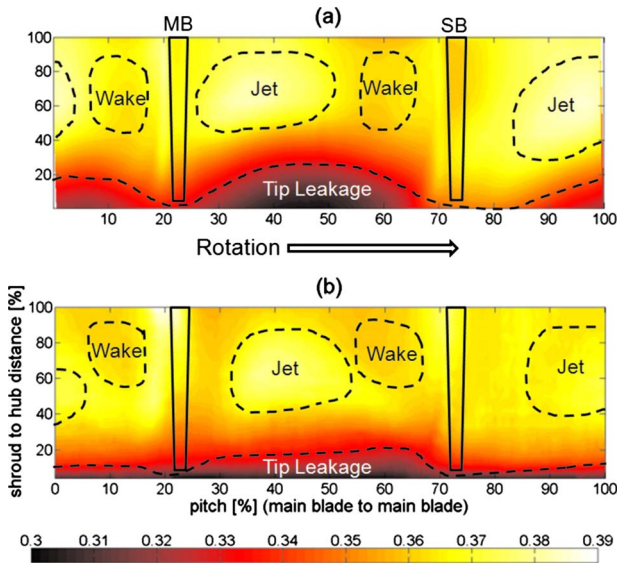

Fig. 6 Total pressure ratio (Mu=0.8 and Q/Q_{ref}=0.55) at impeller exit: (*a*) computational and (*b*) experimental

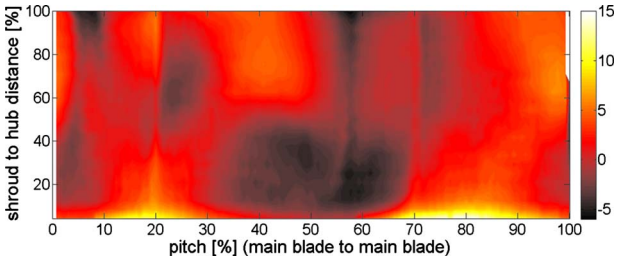

Fig. 7 Relative difference in total pressure ratio: numerical results compared with FRAP measurements (Mu=0.8 and Q/Q_{ref}=0.55)

flow. However, a correct prediction of the resistance line of the facility was not expected owing to the fact that only the impeller is included in the model.

Further validation of the computational model was undertaken on the basis of unsteady flow measurements taken approximately one diffuser height downstream of the impeller exit. A detailed description of the measurement setup, as well as probe dimension, measurement range, and accuracy, is presented by Schleer [14].

Figure 6 shows the total pressure ratio for both the steady state simulation and the flow measurements over one main blade pitch. The results are compared for the speed line termed Mu=0.8 and a mass flow ratio of Q/Q_{ref}=0.55. The trailing edge of the main blade is indicated as "MB" and the splitter blade trailing edge as "SB." The identified jet, wake, and tip leakage flow features correspond to the classical jet-wake model proposed by Dean and Senoo [15]. In general the agreement is good. However, a major difference in the CFD profile compared with the measured values is the formation of the vortical structure caused by tip leakage fluid flow. Within this flow region the low momentum fluid, as predicted by the computation, occupies a significantly bigger portion of the channel and is not confined to the shroud, but penetrates into the bulk flow. Since the mass flow is equal in the simulation and the experiment, the pronounced blockage at the shroud is compensated by increased velocities within the jet regime. In the authors' opinion the main contributor to this disagreement may be inaccuracies in the tip leakage flow modeling. This includes aspects such as tip gap variation along the shroud and meshing within the gap.

The relative difference of the CFD compared with the measured total pressure ratio is in the range of ±5% except for the tip leakage region at the shroud (see Fig. 7). Overall, the difference between prediction and measurement is good and justifies the use of the CFD approach to provide valid predictions of the flow field.

6 Unsteady Results

6.1 Solver Monitoring for Unsteady CFD Computations. In order to assess periodic convergence of the unsteady computations, time-resolved blade pressures were recorded at a number of monitoring points on the surface of a main blade (see Fig. 8). The monitoring points were situated at midheight on both the pressure and suction sides of the main blade at 10%, 50%, and 90% chords. The rate of periodic convergence was quantified by correlating the unsteady pressure traces for each monitoring point over two consecutive impeller revolutions.

Figure 9 shows a typical evolution of the correlation coefficients at all monitoring points during an unsteady CFD run. The resulting correlation coefficients in the presented results for periodic convergence were set to be at least 99% for all the six monitoring locations.

6.2 Effect of Inlet Distortion on Performance. The flow through a centrifugal impeller is highly complex and characterized by separation zones and secondary flows. A dominant source of the secondary flows, which extend into the diffuser, is the tip leakage flow. As discussed, for example, by Schleer [14] the clearance flow, in particular, for the relatively large clearance ratios in highly loaded small scale compressors, is identified as a strong vortical feature. This flow pattern near the shroud destabilizes the compressor and degrades its performance. Bearing this in mind, the effect of inlet flow distortion on the performance of the data impeller was studied.

The comparison of the computed performance between the distorted inlet flow field and the undistorted case is shown in Fig. 10. The operating line was obtained for 16,250 rpm, which approximately corresponds to Mu=1.0. The performance for the undistorted inlet flow field was computed with steady state simulations. In the case of the distorted flow field, the unsteady computation was performed with inlet boundary conditions obtained from five

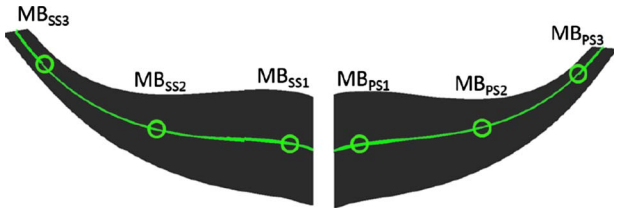

Fig. 8 Monitoring points on main blade surface

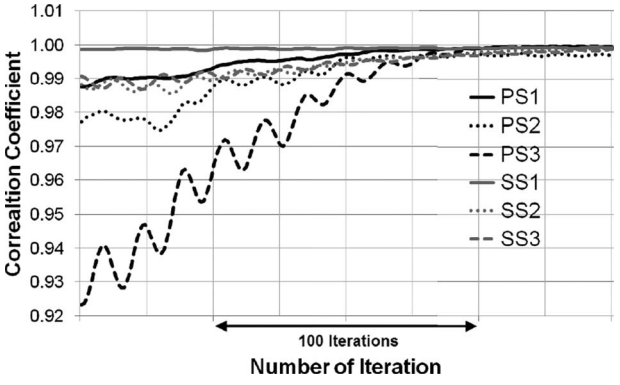

Fig. 9 Evolution of correlation coefficient in unsteady simulation

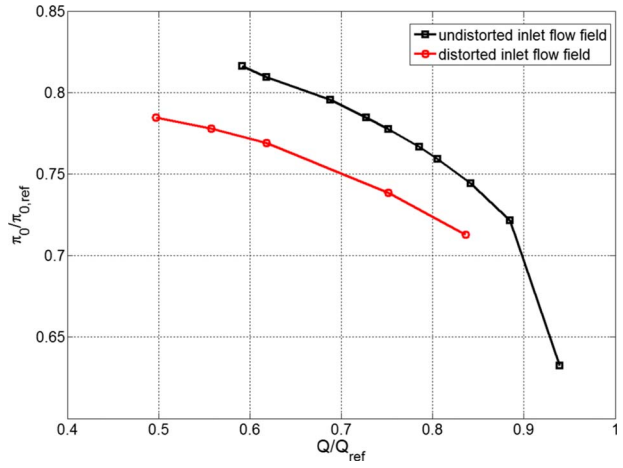

Fig. 10 Comparison of computed performance, 16,250 rpm, 5. EO distortion

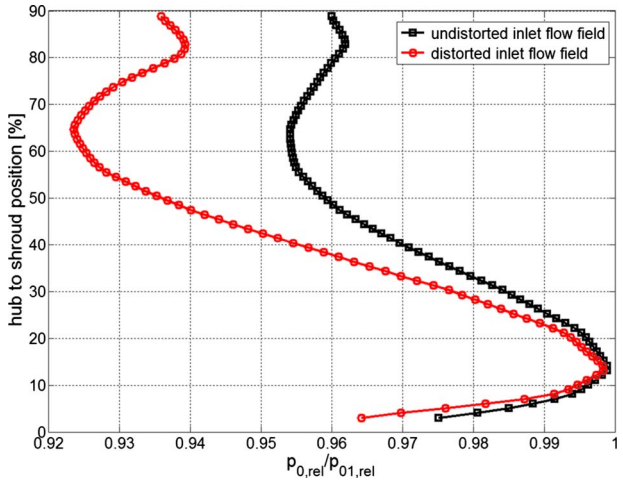

Fig. 11 Total pressure profiles, hub to shroud, impeller exit, 16,250 rpm, Q/Q_{ref}=0.62, 5. EO distortion

lobe screen measurements. Ideally, the comparison should be carried out on the basis of unsteady computations. With regard to undistorted inlet flow, a single operating point comparison of unsteady and steady computations showed equal results in terms of predicted performance. In the authors' opinion, this finding allows the direct comparison of steady computations for the undistorted and unsteady computations for the distorted case. However, a comparison in terms of the operational margin cannot be carried out. In Fig. 10 the decrease in the impeller total pressure ratio of about 6% can be identified as occurring due to inlet flow distortion. With regard to stability, it was possible to simulate operating points below Q/Q_{ref}=0.62 with unsteady CFD while in the case of steady undistorted computations, no stable convergence could be obtained. This observation corresponds to the statement made by Dickmann et al. [8].

In order to assess the causes of performance deterioration, the relative total pressure profiles from hub to shroud were examined. Figure 11 compares the distribution of the relative total pressure loss one diffuser channel height downstream of the impeller exit. The values are based on circumferentially mass flow weighted averaging. The higher total pressure loss at the 50–80% diffuser channel height level coincides with the trace of the shroud gap vortex. The comparison of the relative total pressure profile at Q/Q_{ref}=0.62 for the distorted and the undistorted inlet flow field gives reason to argue that the interaction of the distortion with the tip leakage flow causes additional loss in relative total pressure and leads to the decreased performance of the compressor.

6.3 Unsteady Blade Pressure Distribution. A major objective of the present work was the quantification of the unsteady pressure distribution on the blade surface. The time varying pressure distribution on the blade, caused by the inlet distortion, may excite the modes of the blades. To understand the translation of the distortion created in the inlet section onto the blade surface, it was important to obtain the magnitude and distribution of the dynamic load over the blade surface. The transformation from the time into the frequency domain of the unsteady pressure traces provides information on the amplitude and the frequency content of the forcing function. An illustrative way to visualize the trace of the distortion convecting through the blading is to take a blade to blade view at midspan. As a matter of course, the relative total

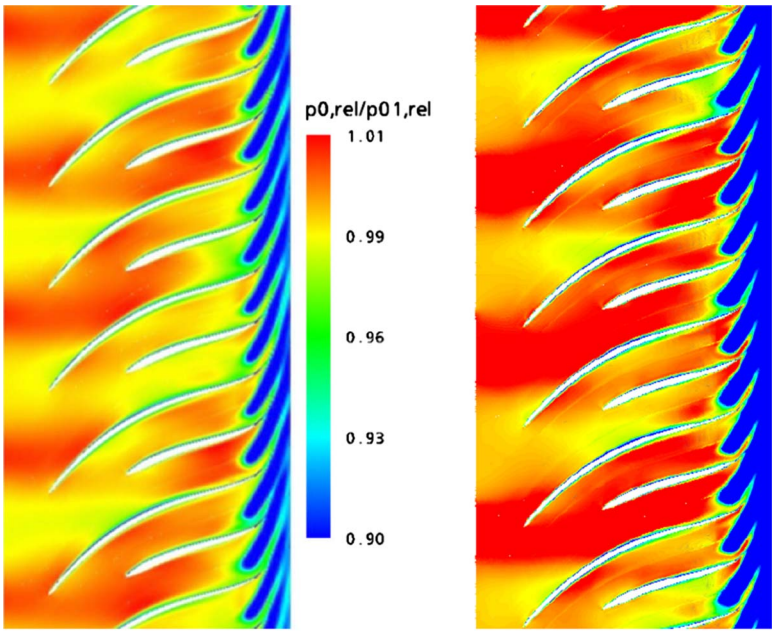

Fig. 12 Relative total pressure at midspan

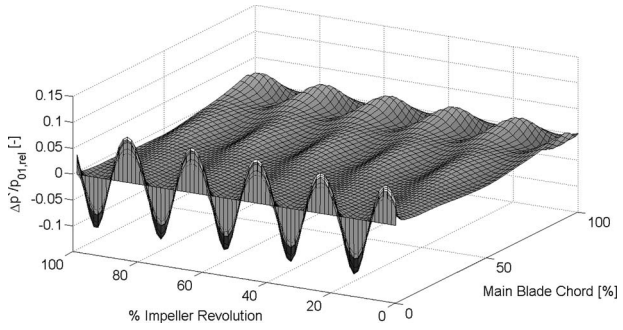

Fig. 13 Path-time diagram, pressure fluctuation (PS-SS), midspan, 5. EO, 16,250 rpm, $Q/Q_{ref}=0.76$

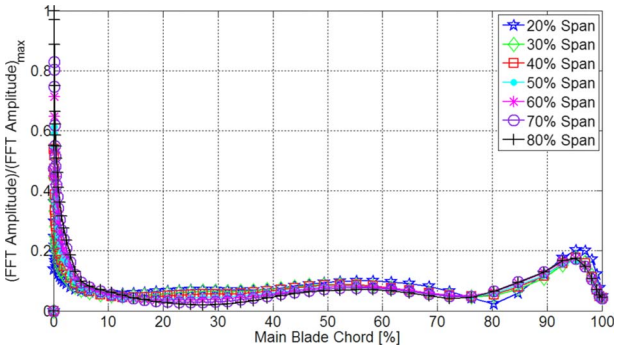

Fig. 15 FFT amplitude [$\Delta p'$], fundamental excitation, 16,250 rpm, $Q/Q_{ref}=0.76$, hub to shroud variation

pressure in the distorted inlet flow is lower compared with the undistorted flow. This way, it is possible to identify the zones of relative total pressure loss (boundary layers, vortical structures, inlet distortion, etc.). The plot on the left in Fig. 12 shows the relative total pressure distribution at midspan for 16,250 rpm using boundary conditions obtained from the five lobe screen. The right plot shows results for 20,700 rpm obtained for the four lobe screen. In both cases the distorted and undistorted portions of the flow field can be identified. The circumferential extent of a low relative total pressure streak corresponds in both cases approximately to a main blade pitch. Within the space between two main blades this leads to a flow pattern, which is either entirely dominated by low momentum or high momentum fluid. In the leading edge region, which is the most sensitive to blade vibration, observations show that high instantaneous pressure differences between the suction and pressure sides are to be expected. For a number of blades high momentum fluid can be identified on one side of the blade whereas at the same time low momentum fluid can be identified on the other side of the blade.

In order to gain further insight into the effect of inlet distortion, the unsteady pressure distribution is plotted in the path-time diagram (Fig. 13), which allows illustration of the distortion convecting along the blade surface. The difference in pressure fluctuation between pressure and suction sides is plotted, from leading to trailing edge at midspan over one impeller revolution.

The integral of the pressure fluctuation over the blade area equals the dynamic load caused by the distorted inlet flow field. It can be observed that the distortion convects through the impeller with almost constant speed. The amplitude decreases between the leading edges of the main blade and the splitter blade and remains almost constant to the trailing edge. These findings confirm that the strongest pressure fluctuations are present in the inducer part of the impeller. Given this flow field the oscillating dynamic load would excite the main blade in its first eigenmode if the frequency of the excitation crosses the resonance frequency. The Fourier transform of the unsteady pressure fluctuation at midspan from the leading to the trailing edge of the main blade (Fig. 14) shows the development of the amplitude and the frequency content as the unsteady flow convects through the impeller.

As expected, the excitation is strongest at the leading edge of the main blade. The second harmonic appears comparatively weak in the leading edge region and is about 15% of the amplitude of the fundamental frequency. The amplitude of the unsteady pressure distribution on the suction side was found to be of similar magnitude to that on the pressure side. Due to the fact that an idealized inlet flow distribution was used as the inlet boundary condition, the fundamental frequency can be seen to dominate the distortion pattern. The amplitude of the second harmonic can be considered to be an artifact of the idealization process. Overall, the applied idealization process of the inlet boundary conditions leads to a sinusoidal excitation function acting on the main blade.

Figure 15 shows the normalized amplitude of the unsteady pressure distribution for several spanwise locations from leading to trailing edge of the main blade. The dynamic load caused by the excitation with the fundamental frequency is high in the inducer section of the main blade and decreases by 50% blade chord to a value below 10% of the maximum amplitude at 80% span. The chordwise position of the peak amplitude can be observed to propagate downstream as the radius increases. This corresponds to an increase in incidence as the blade speed increases. The evolution of the phase angle of the dynamic load is shown in Fig. 16. Over the entire blade span, the excitation with the fundamental frequency is in phase for the front part of the blade. According to findings in Ref. [11] this favors the excitation of the first main blade mode where the mode shape is characterized by in-phase displacement. The phase change in the rear part of the main blade does not significantly affect the excitation of the mode. The formation of a point of inflection at 25% main blade chord for locations above 60% blade span might be the result of an interaction of the tip leakage flow with the distortion pattern convecting through the blading.

6.4 Forcing Function Sensitivity on Change in Mass Flow. From the perspective of the forced response problem, it is crucial

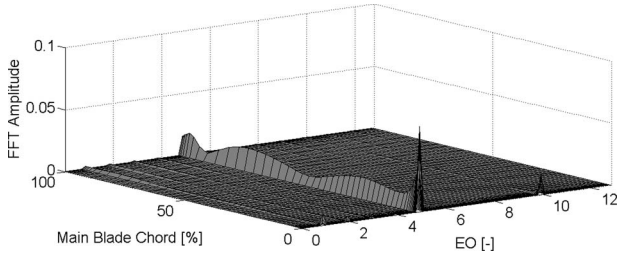

Fig. 14 FFT amplitude of unsteady pressure on PS of MB, 16,250 rpm, $Q/Q_{ref}=0.76$, midspan

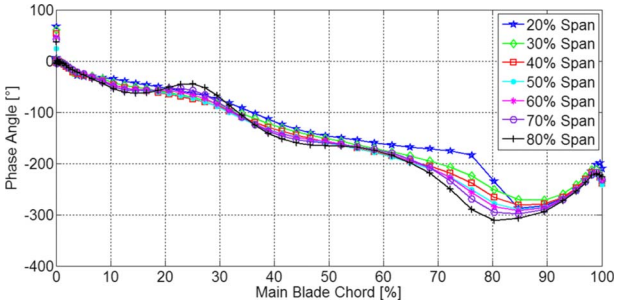

Fig. 16 FFT phase angle (deg), fundamental excitation, 16,250 rpm, $Q/Q_{ref}=0.76$, hub to shroud variation

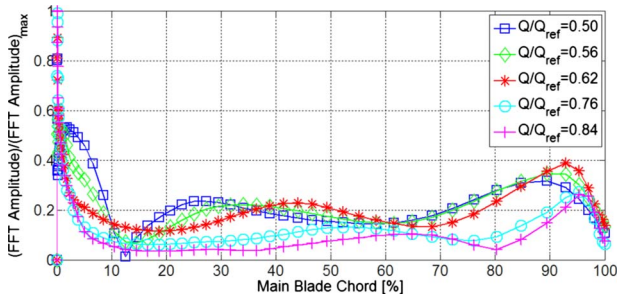

Fig. 17 FFT amplitude [$\Delta p'$], midspan, 5. EO, 16,250 rpm, variable mass flow rate

to understand and quantify the evolution of the forcing function as the mass flow changes for a given resonant speed condition. To do so, unsteady CFD was performed for a number of mass flow settings along the main speed line of 16,250 rpm where resonance with the first main blade mode occurs. Figure 17 shows the nondimensionalized amplitude of the unsteady pressure distribution at midspan on the main blade for five operating points with constant blade speed but varying mass flow rates. In general the maximum of the dynamic load decreased by reducing the mass flow rate. For corrected mass flow ratios of $Q/Q_{ref}=0.62$ and lower, there is a tendency to a kink at about 12% blade chord and a shift of the excitation to a higher chordwise position. The dynamic load increases in the rear part of the main blade for reduced mass flow rates.

The phase shift for the operating point with a corrected mass flow ratio of $Q/Q_{ref}=0.50$ (Fig. 18) is the outcome of the long convection time of the distortion through the impeller at low mass flow rates. The change in phase along the chord is therefore comparatively strong with the forcing function being in phase for the front and rear portions of the blade.

In order to better visualize the change in the trend to lower amplitudes of the fundamental excitation frequency with decreasing mass flow ratios the flow conditions at the leading edge of the main blade are shown in detail. Figure 19 compares the variance of the pressure fluctuation p' for the mass flow ratios $Q/Q_{ref}=0.50$ and $Q/Q_{ref}=0.76$. The comparison shows the evolution of zones with high fluctuation amplitudes of the blade pressure in the front part of the pressure side and at high spanwise levels on the suction side.

The emerging modulation of the forcing function could be explained by looking at the variation of the incidence as a function of the mass flow rate and the distortion of the flow created in the inlet section. Figure 20 shows the relative flow angle at midspan for different mass flow rates compared with the metal angle of the main blade. As soon as the incidence reached positive values for

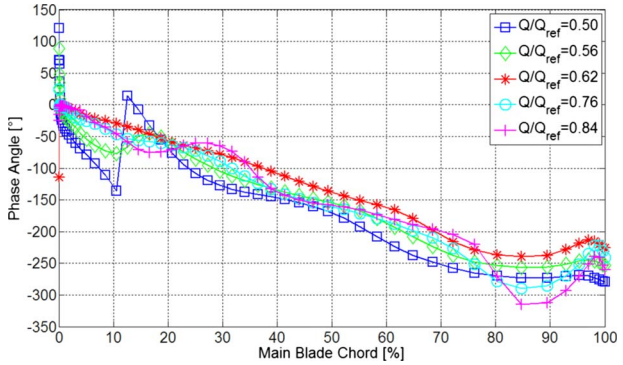

Fig. 18 FFT phase angle (deg), midspan, 5. EO, 16,250 rpm, variable mass flow rate

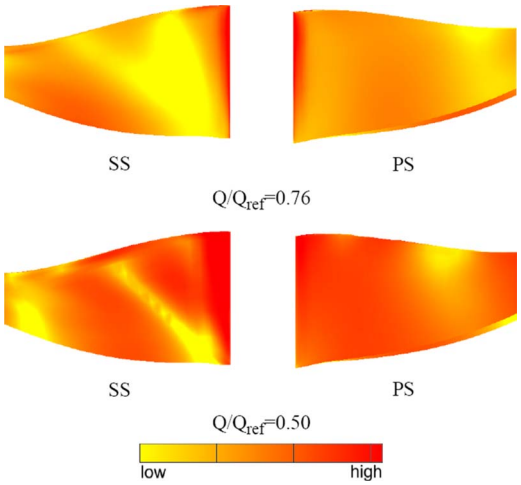

Fig. 19 p'_{rms}, main blade, inducer section

both the high and low momentum zones of the distortion pattern, flow instabilities are predicted on the suction side of the main blade over the entire impeller revolution.

On the suction side of the main blade separation is caused by the high incidence angle and was found to occur for the entire impeller revolution. Thus, close to the stability line, the forcing function is affected by the dynamics of the separation bubble. The operating points at $Q/Q_{ref}=0.56$ and $Q/Q_{ref}=0.62$ showed the transition from the aerodynamically stable to the unstable operating range concerning the main blade inducer section. It seems that the undistorted portion of the inlet flow field stabilizes the whole compressor as long as the associated incidence angle is in the stable range. This observation is consistent with the parallel compressor model proposed by, e.g., Mazzawy [16].

However, the investigation of the stability and the performance of the compressor in the near stall region was not part of the scope of the present work. A detailed discussion would therefore require additional investigation. Toward low incidence angles, i.e., when the flow rate was increased, flow instabilities on the pressure side could not be detected in the unsteady computation.

6.5 Comparison Between Idealized and Real Inlet Boundary Condition. Due to the use of an ideal inlet total pressure boundary condition, frequencies below and above the fundamental excitation frequency of the screen were eliminated. These frequencies were generated due to strut arrangements in the inlet section of the impeller. The following results aim to compare unsteady computations with idealized and real boundary conditions. To start with, Fig. 21 shows the inlet boundary condition where the missing sectors were fitted. The flow field can be observed to be subject to comparatively strong fluctuations in circumferential and radial directions.

The computation was processed in the same way as previously outlined and the frequency content of the pressure fluctuation at midspan was then examined (Fig. 22). The results reveal a number of frequencies to be present in the forcing function. In terms of amplitude, the third engine order is approximately half as strong as the fundamental frequency (fifth engine order). The relative strength of the third engine order was expected since inlet flow measurements without a distortion screen clearly showed this frequency to dominate the inlet flow field.

The evolution of the amplitude in Fig. 23 shows good consistency of the trend in a chordwise direction. However, the magnitude of the excitation with the real boundary condition is lower by about 30% compared with the ideal case. This is more apparent when comparing the total pressure distribution in a circumferential direction for the two profiles (Figs. 3 and 21). The evolution of the phase angle was found to be identical for the two cases. The

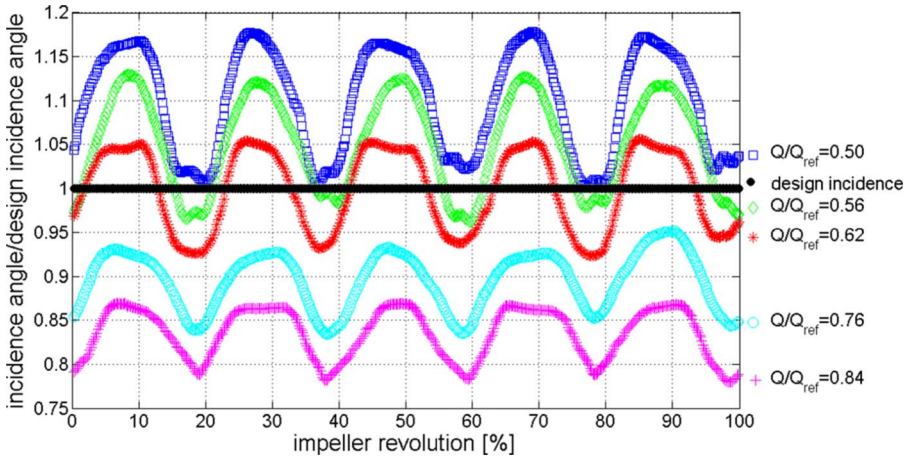

Fig. 20 Incidence angles, midspan, main blade, 16,250 rpm, 5. EO

reduction in the amplitude in the real case and the content of the lower order frequencies in the distorted inlet flow field have to be taken into account when these results are used to interpret and understand data obtained from strain gauge measurements in the facility. The lower order frequencies may interact with the intended fundamental excitation and may cause amplification or damping during blade vibration.

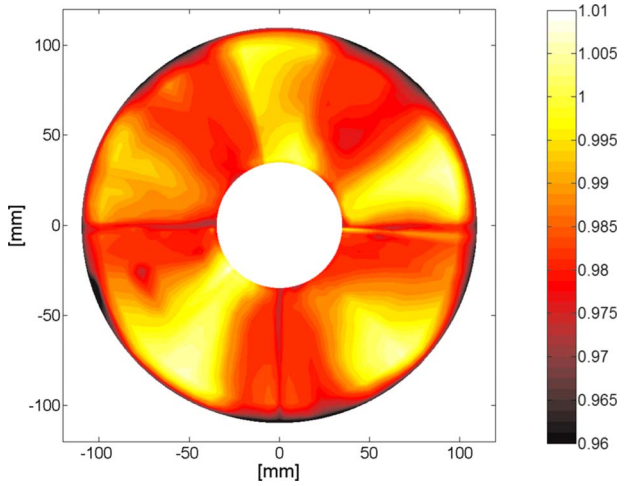

Fig. 21 Real inlet total pressure boundary condition distribution p_0/p_{01}, 5. EO

7 Summary and Conclusions

The computations aimed to quantify the forcing function acting on the blade surface due to inlet flow distortion. The detailed validation of the model on the basis of steady state simulations showed reasonable consistence with the test rig performance. The deviations in performance were of the order of 2% over the whole compressor map. The comparison of the total pressure distribution at the exit of the impeller from hub to shroud with FRAP measurements confirmed the prediction of the CFD results. Deviations of the order of 10% between prediction and measurements were detected at the shroud where the flow is dominated by the tip leakage flow. During unsteady computation measured inlet boundary conditions were applied. Periodic convergence was achieved and was assessed by correlating pressure fluctuations on the blade surface for consecutive revolutions. In terms of performance, the total pressure rise across the impeller was found to degrade by about 6% in the case of inlet flow distortion for the speed line where resonance occurs between the first main blade mode and fundamental excitation frequency of the distortion screen. In terms of stability, periodic convergence for the unsteady computations could be achieved at lower mass flow rates compared with the steady computations. The analysis of the unsteady pressure distribution showed that the highest amplitudes occur in the inducer part of the blade. However, the amplitude was found to depend on the mass flow rate. Decreasing the mass flow resulted in a decrease in maximum pressure fluctuation. Toward the impeller stability line the increase in incidence caused separation on the suction side of the blade and therefore considerably altered the

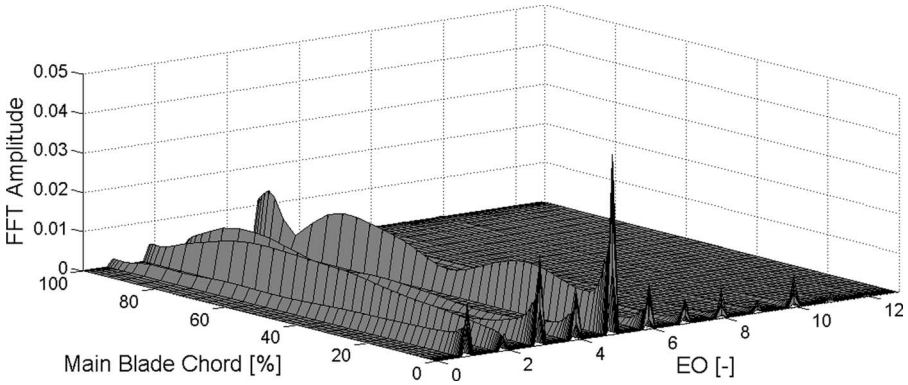

Fig. 22 FFT amplitude of unsteady pressure on PS at midspan, 16,250 rpm, Q/Q_{ref} =0.76, real inlet total pressure boundary condition distribution

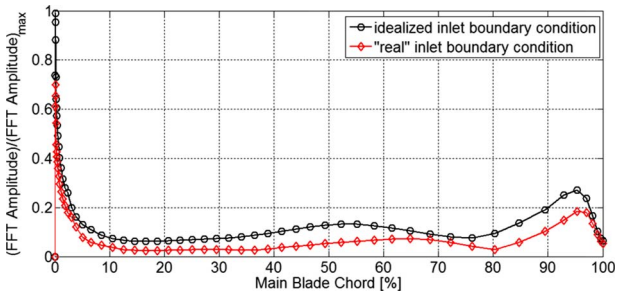

Fig. 23 FFT amplitude [$\Delta p'$], midspan, 16,250 rpm, 5. EO, $Q/Q_{ref}=0.76$, idealized versus real inlet total pressure boundary conditions

amplitude and the phase angle of the unsteadiness. Overall, results show that the forcing function is most sensitive at the leading edge of the blade and might therefore affect the blade response amplitude during forced vibration. A study of the effect of idealizing the inlet flow distribution on the forcing function was carried out. In the case of the idealized boundary conditions the frequency content is reduced to the fundamental frequency of the distortion screen whereas in the other case additional frequencies were present. A comparison of the amplitude of the fundamental excitation frequency showed that in the idealized case the amplitude is higher by up to 30% since modulation due to lower frequencies is not present. In the authors' opinion idealized inlet boundary conditions can be used for case studies and to capture trends. However, computations should be carried out for comparison.

Nomenclature

b = diffuser width (m)
CFD = computational fluid dynamics
EO = engine order
FFT = fast Fourier transform
Mu = stage Mach number $U_2/\sqrt{\gamma RT_1}$
$\dot{m}$ = mass flow rate (kg/s)
Q = corrected mass flow rate $\dot{m}\sqrt{T_0/p_0}$
$\dot{V}$ = volumetric flow rate (m^3/s)
PS = pressure side
p = static pressure (Pa)
p_0 = total pressure (Pa)
R = gas constant (J/K mol)
SS = suction side
t = tip clearance width (m)
T = static temperature (K)
T_0 = total temperature (K)
U = blade speed (m/s)

Greek

γ = heat capacity ratio
π = static to total pressure ratio of compressor stage
π_0 = total pressure ratio of compressor stage

Superscripts

$(\cdots)'$ = fluctuation

Subscripts

ref = quantities at design operating point
rel = quantities in relative frame of reference
rms = quadratic mean
1 = impeller inlet
2 = impeller exit

References

[1] Came, P. M., and Robinson, C. J., 1999, "Centrifugal Compressor Design," Proc. Inst. Mech. Eng., Part C: J. Mech. Eng. Sci., **213**, pp. 139–155.
[2] Borgogno, R., and Barmpalias, K. G., 2008, "Evaluation and Optimization of a Novel Aero Engine Cycle," Semester Project, Turbomachinery Laboratory, ETH Zurich.
[3] Srinivasan, A. V., 1997, "Flutter and Resonant Vibration Characteristics of Engine Blades," ASME J. Eng. Gas Turbines Power, **119**(4), pp. 742–775.
[4] Greitzer, E. M., Tan, C. S., and Graf, M. B., 2004, *Internal Flow Concepts and Applications*, Cambridge University Press, Cambridge.
[5] Cumpsty, N. A., 2004, *Compressor Aerodynamics*, Krieger, Malabar, FL.
[6] Ariga, I., Kasai, N., Masuda, S., Watanabe, Y., and Watanabe, I., 1983, "The Effect of Inlet Distortion on the Performance—Characteristics of a Centrifugal Compressor," ASME J. Eng. Power, **105**, pp. 223–230.
[7] Engeda, A., Kim, Y., Aungier, R., and Direnzi, G., 2003, "The Inlet Flow Structure of a Centrifugal Compressor Stage and Its Influence on the Compressor Performance," ASME Trans. J. Fluids Eng., **125**, pp. 779–785.
[8] Dickmann, H. P., Wimmel, T. S., Szwedowicz, J., Filsinger, D., and Roduner, C. H., 2006, "Unsteady Flow in a Turbocharger Centrifugal Compressor: Three-Dimensional Computational Fluid Dynamics Simulation and Numerical and Experimental Analysis of Impeller Blade Vibration," ASME J. Turbomach., **128**(3), pp. 455–465.
[9] Kupferschmied, P., Köppel, P., Gizzi, W. P., Roduner, C., and Gyarmathy, G., 2000, "Time-Resolved Flow Measurements With Fast-Response Aerodynamic Probes in Turbomachines," Meas. Sci. Technol., **11**, pp. 1036–1054.
[10] Pfau, A., Schlienger, J., Kalfas, A. I., and Abhari, R. S., 2003, "Unsteady, 3-Dimensional Flow Measurements Using a Miniature Virtual 4-Sensor Fast Response Aerodynamic Probe (FRAP)," ASME Paper No. GT2003-38128.
[11] Kammerer, A., and Abhari, R. S., 2008, "Experimental Study on Impeller Blade Vibration During Resonance—Part 1: Blade Vibration Due to Inlet Flow Distortion," ASME Paper No. GT2008-50466.
[12] Schleer, M., Mokulys, T., and Abhari, R. S., 2003, "Design of a High Pressure-Ratio Centrifugal Compressor for Studying Reynolds Number Effects," IMechE Conf. Trans., **4**, pp. 391–404.
[13] ANSYS, Inc., 2004, CFX-5.7 User Manual.
[14] Schleer, M., 2006, "Flow Structure and Stability of a Turbocharger Centrifugal Compressor," Fortschr.-Ber. VDI Reihe 7 Nr. 484, VDI Verlag, Düsseldorf.
[15] Dean, R. C., and Senoo, Y., 1960, "Rotating Wakes in Vaneless Diffusers," ASME J. Basic Eng., **82**, pp. 563–574.
[16] Mazzawy, R. S., 1977, "Multiple Segment Parallel Compressor Model for Circumferential Flow Distortion," ASME J. Eng. Power, **99**(2), pp. 288–296.